Cellular and Molecular Bioengineering
https://doi.org/10.1007/s12195-023-00789-5

BMES BIOMEDICAL ENGINEERING SOCIETY

ORIGINAL ARTICLE

Three-Dimensional Fractal Analysis of the Interstitial Cells of Cajal Networks of Gastrointestinal Tissue Specimens

Sue Ann Mah[1] · **Recep Avci**[1] · **Jean-Marie Vanderwinden**[2] · **Peng Du**[1]

Received: 10 March 2023 / Accepted: 14 November 2023

Abstract

Introduction Several functional gastrointestinal disorders (FGIDs) have been associated with the degradation or remodeling of the network of interstitial cells of Cajal (ICC). Introducing fractal analysis to the field of gastroenterology as a promising data analytics approach to extract key structural characteristics that may provide insightful features for machine learning applications in disease diagnostics. Fractal geometry has advantages over several physically based parameters (or classical metrics) for analysis of intricate and complex microstructures that could be applied to ICC networks.

Methods In this study, three fractal structural parameters: Fractal Dimension, Lacunarity, and Succolarity were employed to characterize scale-invariant complexity, heterogeneity, and anisotropy; respectively of three types of gastric ICC network structures from a flat-mount transgenic mouse stomach.

Results The Fractal Dimension of ICC in the longitudinal muscle layer was found to be significantly lower than ICC in the myenteric plexus and circumferential muscle in the proximal, and distal antrum, respectively (both $p < 0.0001$). Conversely, the Lacunarity parameters for ICC-LM and ICC-CM were found to be significantly higher than ICC-MP in the proximal and in the distal antrum, respectively (both $p < 0.0001$). The Succolarity measures of ICC-LM network in the aboral direction were found to be consistently higher in the proximal than in the distal antrum ($p < 0.05$).

Conclusions The fractal parameters presented here could go beyond the limitation of classical metrics to provide better understanding of the structural-functional relationship between ICC networks and the conduction of gastric bioelectrical slow waves.

Keywords Bio-image analysis · Fractal analysis · Neurogastroenterology & motility · Pacemaker cells · Interstitial cells of Cajal (ICC) network structure · Gastric antrum · Lacunarity · Succolarity

Introduction

Interstitial cells of Cajal (ICC) are specialized pacemaker cells distributed throughout the gastrointestinal (GI) tract. ICC networks generate rhythmic bioelectrical events known as slow waves (SWs) and aid in the coordination of motility [19, 33]. Characterization of the complex microstructure of ICC networks and the relation between the structural properties and GI function in health and disease is an emerging area of research [8, 9, 25]. Differences in ICC network microstructure are often a fundamental factor for predicting the macroscopic physiology of GI motility function.

Specific structural traits such as deficient, and/or altered networks of ICC are often observed in gastroparesis [15], constipation [16], chronic intestinal pseudo-obstruction [20], and Hirschsprung disease [35]; based on qualitative histopathological findings, and serve as key factors in inferring the health of GI motility function. Although confocal microscopy can image and quantify the spatial distribution of ICC networks, current techniques to evaluate ICC in histological studies are limited to nuclei counts, volume computations, or, most often, simply by visual grading [25]. A

Associate Editor Jennifer Linderman oversaw the review of this article.

✉ Sue Ann Mah
smah113@aucklanduni.ac.nz

✉ Peng Du
peng.du@auckland.ac.nz

[1] Auckland Bioengineering Institute, The University of Auckland, Auckland, New Zealand

[2] Laboratoire de Neurophysiologie, Faculté de Médecine, Université Libre de Bruxelles, Brussels, Belgium

Published online: 27 November 2023

critical advance would be to develop an objective, automated techniques for the quantitative assessment of ICC networks. A suite of numerical metrics for the quantitative assessment of the structural features of ICC networks has recently been developed [9, 28]. However, analysis has been limited to the analysis of ICC structure in two-dimensional images.

Since Mandelbrot proposed fractal geometry in the 1970s, [29] it has since been widely applied across multiscale structural analysis in various fields and has been extended to characterize physiological processes and anatomical structures [12]. Fractal geometry theory includes several key structural parameters including Fractal Dimension (FD), Lacunarity, and Succolarity [29]. FD indicates how and by how much an object occupies its underlying metric space; and is an important parameter to characterize scale-invariant physical properties. The FD has been widely used to characterize the complex retinal vasculature of retinopathy [30], pulmonary bronchial and vascular trees [32], and neuronal cellular profiles [36]. Lacunarity evaluates the degree of gap distribution within a structure and therefore describes the heterogeneity in the distribution of gap sizes [11]. Succolarity evaluates the degree of filaments that allow percolation of a medium [6], and characterizes the extent of connectedness or anisotropy for a given direction [43]. Both Lacunarity and Succolarity can distinguish different structures with the same FD.

In contrast to numerous research applications pertaining to FD, there have been relatively few studies performed with Lacunarity and Succolarity on biological structural analysis for clinical applications, with none to date on ICC networks. Recent studies have explored the implementation of (multi) fractal analysis and Lacunarity for the quantitative characterization of the microvascular geometry in the retina [1, 14, 31, 34]. The results of these studies demonstrated the classification between normal, developing, and pathological tissues with high specificity, with the potential of translating to diagnostic biomarker. Krohn et al. [23] computed FD estimates on global tissue segmentations of structural brain MRI, and demonstrated its potential as a marker in a wide range of vascular, inflammatory, neoplastic, and neurodegenerative pathologies. Likewise, these fractal structural parameters can be employed to quantify the complex, intricate structures of the ICC networks from different regions of the GI tract.

In this paper, FD, Lacunarity, and Succolarity were investigated based on the box-counting methods and gliding-box algorithm [39, 42], on confocal images of transgenic mouse gastric tissues [22]. The implementations of the algorithms were validated with standard self-similar classical 3D fractal structures.

Methods

Whole-Mount ICC Image Acquisition & Segmentation

A previously reported wholemount transgenic mouse stomach images of ICC was used [22]. Ethical approval was provided by the Université Libre de Bruxelles Animal Welfare Committee (Protocols 491N and 552N). A whole-mount tissue sample was obtained from the stomach antrum of a 10-week-old male (c-KitCreERT2, R26mT-mG) transgenic mouse that expressed enhanced green fluorescent protein in the c-Kit positive cells after administration of tamoxifen [22]. C-Kit is a receptor tyrosine kinase, which is specifically expressed in ICC within the gut musculature and serves as a fiducial marker for ICC [40].

Two groups of transverse image tiles (identified in this paper as the proximal and distal tiles) were acquired using a multiphoton microscope (LSM780NLO, Zeiss, Jena, Germany) with an excitation wavelength of 920 nm, LD C-Apochromat 40x/1.1 water immersion objective, and a digital zoom of 0.7. Emission was collected in 3 channels-second-harmonic generation (SHG), green channel, and red channel consisting of emission wavelengths between 445–470 nm, 500–545 nm, and 570–620 nm; respectively. Only the green channel expressing green fluorescence protein (GFP) c-Kit positive ICC was used in the analysis in this study. Frames of 512×512 pixels with a field of view of 303×303 μm^2 were acquired as an image stack with 1 µm spacing across the thickness of the gastric wall. The proximal ($6170 \times 862 \times 285$ μm^3) and distal ($5611 \times 862 \times 266$ μm^3) tiles were composed of a grid of image stacks with 8% overlap and their approximate locations are illustrated in Fig. 1a. A total of 126 whole-mount image stacks were analyzed in this study. The proximal region was comprised of stacks of images (n = 66). ICC-MP and ICC-CM were observed in all image stacks, while ICC-LM was only observed in 32 image stacks- ICC-LM (n = 32), ICC-MP (n = 66), and ICC-CM (n = 66). The distal region was comprised of stacks of images (n = 60), five of which, were excluded from the analysis due to poor image quality; resulting in, ICC-LM (n = 38), ICC-MP (n = 55), and ICC-CM (n = 55).

All 126 tissue stacks were segmented using the Weka Fast Random Forest (FRF) model machine learning classifier as described previously [28]. An example of the segmented image stack is shown in Fig. 1c, where the ICC-LM, ICC-MP, and ICC-CM layers are visible. Examining the confocal image stacks from the serosal to the mucosal surface: the ICC-LM is located closest to the serosal surface, followed by the ICC-MP and ICC-CM, as

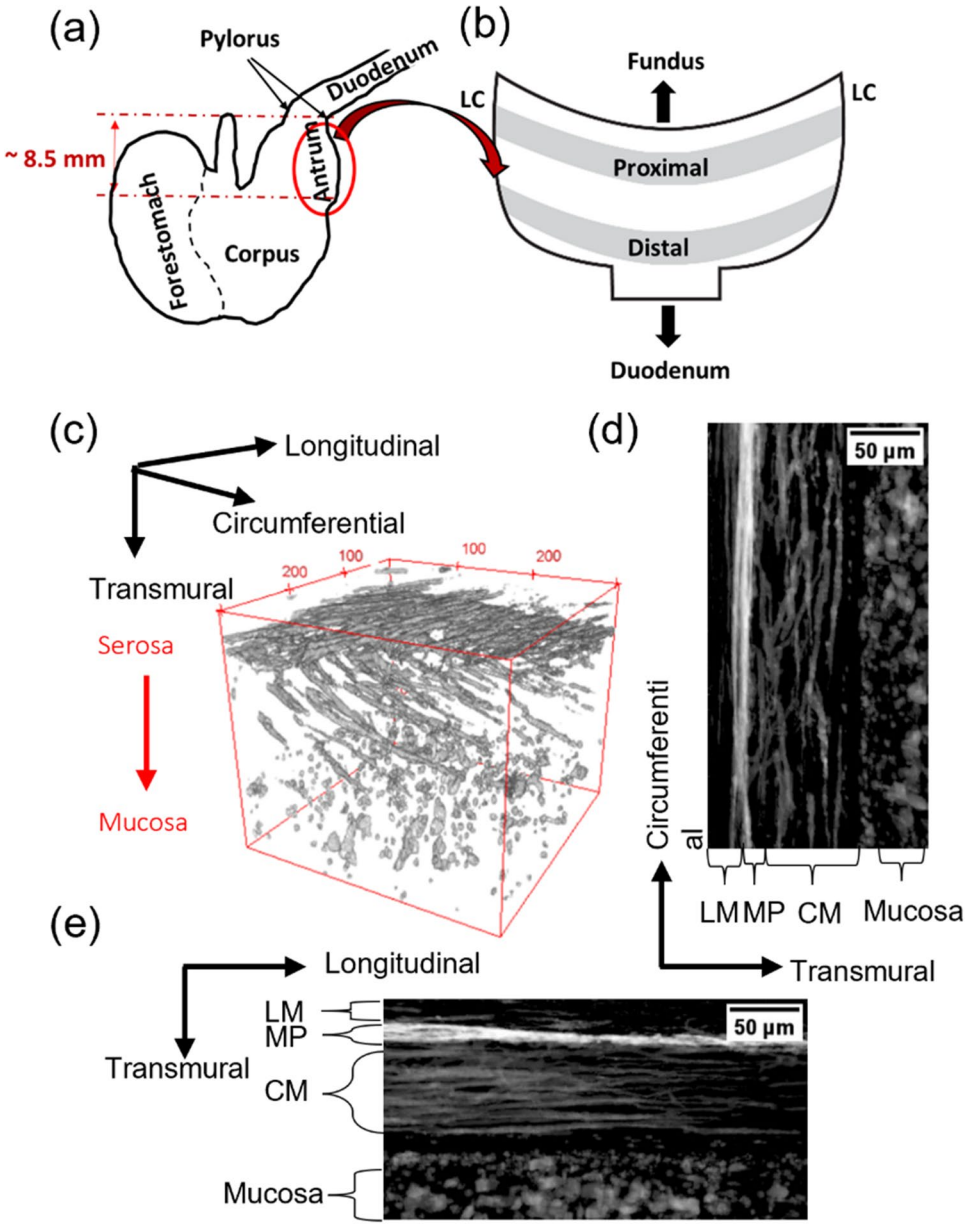

Fig. 1 ICC network morphology of the mouse gastric antrum following machine learning segmentation of confocal imaged ICC. **a** The antrum was dissected along the lesser curvature, and **b** the approximate location of two transverse tissue strips (proximal and distal) within the mouse gastric antrum is shown. **c** An isometric view of a single image stack from the transverse distal strip near the greater curvature. **d** Circumferential-projection of the segmented image stack based on the standard deviation of pixels along the longitudinal-transmural plane, and **e** longitudinal-projection along the circumferential-transmural plane. The ICC-LM, ICC-MP, and ICC-CM can be observed within the longitudinal muscle (LM), myenteric plexus (MP), and circumferential muscle (CM) layers, respectively

observed in Fig. 1c. When projections of the segmented confocal image stacks along the longitudinal direction (Fig. 1d) and circumferential direction (Fig. 1e) are viewed, it is evident that the MP layer contains significantly denser ICC than the surrounding tissue layers [26]. The thickness of each tissue layer along the gastric wall was manually demarcated for each image stack [26]. Variations in the density of ICC could be visually observed along the transmural direction from the circumferentially and longitudinally-projected 2D images (Fig. 1d, e, respectively).

ICC Network Fractal Analysis

Fractal Dimension

The FD indicates how much an object occupies its underlying metric space [6]. Fractal analysis was performed by employing the Hausdorff-Besicovitch 3D box-counting algorithm [2, 42] which involved partitioning the FRF segmented binary image of the ICC networks into several grids of cubes of equal size of $\varepsilon \times \varepsilon \times \varepsilon$ pixels. The procedure was performed for different ε values ranging from 2 to 512 pixels in increments of

powers of 2. Boxes containing at least one ICC voxels were considered positive while those without any ICC voxel were considered negative. The count of positive boxes (N_{pos}) is given, as follows,

$$N_{pos}(\varepsilon) \approx \varepsilon^{-D_0} \tag{1}$$

$$log_{10}\left(N_{pos}(\varepsilon)\right) = -D_0 log_{10}(\varepsilon) + FA \tag{2}$$

where FA denotes fractal abundance. D_0 and FA are defined as the slope and intercept of the linear regression of the log-log plot of $N_{pos}(\varepsilon)$ versus ε, respectively.

FD analysis was performed on sampled ICC-LM, ICC-MP and ICC-CM networks from a confocal image stack. An array of N_{pos} values corresponding to the various cubic box-sizes (i.e., ε = 1,2,4,8,16,32, 64, 128, 256, 512) for each type of ICC network, respectively were computed. With reference to Eq. (1), the number of positive boxes, $N_{pos}(\varepsilon)$ versus box-size, ε for the identified ICC-LM, ICC-MP, and ICC-CM networks from a confocal stack were plotted on a log-log graph, thus, resulting in a linear regression with the slope, D_0 corresponding to the fractal dimensions of ICC-LM, ICC-MP, and ICC-CM networks, respectively. The fractal analysis was then subsequently performed for all the other sampled ICC-LM, ICC-MP, and ICC-CM networks from 126 confocal stacks across the proximal (n = 66) and distal (n = 60) murine antrum.

Lacunarity Analysis

The Lacunarity analysis provides further insights that complements the FD for the quantitative characterization of the ICC networks and can be used to identify the extent of heterogeneity in the distribution of hole sizes surrounding the ICC within its network structure. Lacunarity analysis was performed using our custom MATLAB program based on the 3D gliding box algorithm [39]. The gliding box algorithm was implemented by shifting an ε × ε × ε cube starting at the top left top corner of a 3D image stack and counting the number of ICC voxels within the cube. The process was repeated as the cube was shifted by one voxel to the right each time until it reached the bottom right corner of the image stack and thereafter, the cube is shifted one voxel in the transmural direction [39]. The process was recursively executed until the cube has shifted through all voxels in the confocal image stack. The Lacunarity, L(ε) for a given cube width, ε is calculated as:

$$L(\varepsilon) = \frac{N(\varepsilon) \times Q_2}{Q_1^2} \tag{3}$$

$$Q_1 = \sum_i p(i, \varepsilon) \tag{4}$$

$$Q_2 = \sum_i p(i, \varepsilon)^2 \tag{5}$$

where $N(\varepsilon)$ is the total number of gliding cubes of width ε given the size of the image, x × y × z as; $N(\varepsilon) = (x - \varepsilon + 1)(y - \varepsilon + 1)(z - \varepsilon + 1)$. Q_1 is the sum of the number of signal voxels in each cube, Q_2 is the sum of the square of the number of signal voxels in each cube, and p(i,ε) is the number of signal voxels on the i^{th} cube with i ∈ [1, N(ε)].

An array of $L(\varepsilon)$ values corresponding to different cubic gliding box sizes, ε (i.e. ε = 2,4,8,…,E, with ε being powers of 2, E ≤ N_{min}, and N_{min} representing the minimum dimension of the sampled ICC network) is obtained for each type of ICC network (ICC-LM, ICC-MP, ICC-CM) from a confocal image stack. The Lacunarity plots ($L(\varepsilon)$ vs. ε) for ICC-LM, ICC-MP, and ICC-CM networks from each confocal stack were plotted on a log-log graph. Fitting of the Lacunarity plot was performed during the validation step ("Algorithm Verification" section), whereby we found best resembles that of the power law function. Taking the logarithm of the power law function, thereby, the Lacunarity plot is a straight line on a log-log graph.

The Lacunarity analysis over all cohort sets of ICC-LM, ICC-MP and ICC-CM networks from the 126 confocal stacks were performed. Subsequently, the mean Lacunarity,$L(\varepsilon)$ of ICC-LM (n = 42), ICC-MP (n = 121), and ICC-CM (n = 121); of the 66 proximal and 60 distal cohort sets of confocal stacks, respectively was plotted over the range of gliding box-sizes, ε as log-log plots with error bars representing the standard error (Fig. 5). Each confocal stack was assigned 9 values of ε and curve of best fit was determined from L(ε) against ε when plotted on a $\log_{10}$-$\log_{10}$ scale. With reference to Eq. (12), the exponent, b, which we use to represent the Lacunarity parameter, corresponds to the slope of the Lacunarity log-log plot. Thus, the Lacunarity parameter, b was evaluated for each of the best fit linear plots as shown in Fig. 5.

Succolarity Analysis

The Succolarity measure serves as another insightful fractal parameter for the quantitative assessment and characterization of the ICC networks. It is used to evaluate the degree of connectivity of a structure in different directions. In the present context, it may characterize the ability of SWs to actively propagate within the gastric tissue. Namely, it quantifies the extent that SWs can actively conduct through the ICC network with respect to a particular direction. The Succolarity analysis was extended based on our previously reported 2D analysis method [27]. In this first step, all ICC voxels, starting from a boundary, have their neighbours (i.e. top, bottom, left, right, front, and back) considered onto the

next step and the process was iteratively executed until it reaches the opposing side of the boundary (e.g., from serosa boundary towards the mucosa boundary). At the conclusion of this step, we will have obtained an intermediate image representing the connected regions in white voxels for each of the 6 directions analysed- serosa to mucosa (s2m), mucosa to serosa (m2s), anterior to posterior (a2p), posterior to anterior (p2a), aboral, and oral.

The intermediate image with dimensions $n_x \times n_y \times n_z$ was then divided into N_σ equal sized boxes by a dividing factor (d). The box size (BS) for a given d is given as:

$$BS(d) = \frac{n_x}{d} \times \frac{n_y}{d} \times \frac{n_z}{d} = \varepsilon_x \times \varepsilon_y \times \varepsilon_z \tag{6}$$

The total number of boxes, N_σ possible in the image for a given d is given as:

$$N_\sigma(d) = d \times d \times d \tag{7}$$

Subsequently, the occupation percentage (OP) of ICC voxels at each level of d was calculated:

$$OP(BS) = \frac{numberof\ \text{ICC}\ voxels}{\varepsilon_x \times \varepsilon_y \times \varepsilon_z} \tag{8}$$

The Succolarity for a given BS is the OP of that box multiplied by its electrical potential, P, which denotes the distance between the centroid (pc) of each BS to the edge from which SW is assumed to propagate from. The direction (*dir*) used in the analysis have influence on the Succolarity results (i.e., the potential field, P increases from top to bottom when considering the serosa to mucosa direction). For anterior-posterior field of potential, the circumferential-position of the centroid was used, while for the aboral-oral field of potential, longitudinal-position of the centroid was used, and for the serosa-mucosa field of potential, transmural-position of the centroid was used.

Therefore, for a given BS and *dir*, the Succolarity (σ) measure is given as:

$$\sigma(BS(d), dir) = \sum_{1}^{N_\sigma} OP(BS(d)) \times P(BS(d), pc, dir) \tag{9}$$

where the direction, *dir* for a given GI confocal tissue can be from serosa to mucosa (s2m), mucosa to serosa (m2s), anterior to posterior (a2p), posterior to anterior (p2a), proximal to distal (aboral), and distal to proximal (oral). The Succolarity value was normalized by dividing the value obtained in Eq. (9) by its largest possible value,

$$\hat{\sigma}(BS(d), dir) = \frac{\sigma(BS(d), dir)}{\sum_1^N P(BS(d), pc, dir)} \tag{10}$$

The overall Succolarity was approximated as:

$$\hat{\sigma}_{avg} = \frac{1}{6} \sum_{dir} \sum_{d=2}^{n} \frac{\hat{\sigma}(BS(d), dir)}{N_\sigma(d)} \tag{11}$$

We notice that Succolarity of ICC networks shows little dependency on BS as observed in our preliminary study [27]. Thus, to improve computational efficiency, we only perform Succolarity analysis for a single BS (d = 2) in this study.

Statistical Analysis

Statistical analysis was performed in MATLAB (R2020b, MathWorks, Natick, MA, USA). Unless otherwise specified, data are reported in mean ± standard deviation. A one-way ANOVA was applied to each quantitative metric to determine a significant difference between ICC-LM, ICC-MP, and ICC-CM within the proximal and distal antrum regions, respectively. Where significance was found, a post-hoc test with Bonferroni correction was performed to reveal pairwise differences. A two-sample t-test or Mann-Whitney U test was performed to determine the specific relationship of statistical significance further between proximal and distal ICC. The adjusted $p < 0.05$ was considered statistically significant.

Results

Algorithm Verification

The fractal analysis algorithm was validated by calculating the FD and Lacunarity of standard self-similar classical fractal-structures. Figure 2a shows the Sierpinski-Menger sponge of the 1st order, 2nd order, and 3rd order.

The computation methods for the FD, Succolarity and Lacunarity as detailed in this paper were based on the Hausdroff box-counting method and the gliding box algorithm. Thus, the box-counting algorithm was validated by comparing the FD results for the yellow fractal phase of the 1st order Menger sponge (FD = 2.7594), 2nd order Menger sponge (FD = 2.6759) and 3rd order Menger sponge (FD = 2.5986) from our program with the ideal FD value of 2.7268 [5] (Fig. 2a); resulting in an RMSE of 0.0819. Therefore, this confidently demonstrates the validity of our box-counting program for calculating the fractal dimension.

After verifying the box-counting method for the FD analysis, the next step was to verify the gliding box algorithm and the calculation of Lacunarity based on Eq. (3). Figure 2c depicts a graph of the Lacunarity values, L(ε) computed at 5 different cubic gliding box widths(i.e., ε = 2, 4, 8, 16, 32) for the 1st order, 2nd order, and 3rd order Sierpinski-Menger sponge, respectively. The Lacunarity plots resembled a power law, therefore, the Lacunarity function was

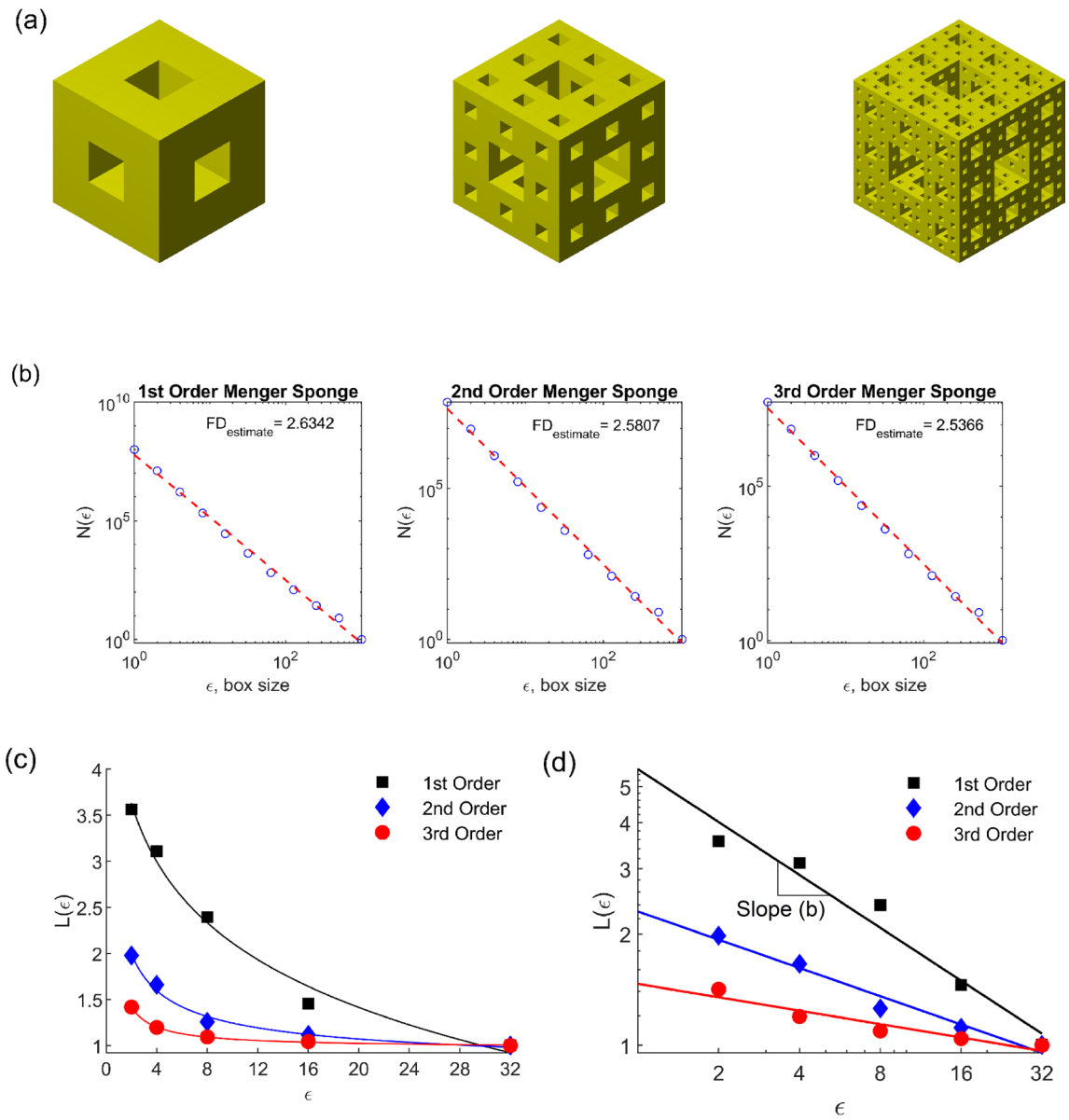

Fig. 2 Fractal and Lacunarity analysis validation. **a** Representation of the first-, second- and third-order Sierpinski-Menger Sponges (left to right). **b** Fractal Dimension estimation based on the linear regression of the log-transformed data for the 3 Menger sponges respectively as shown in **a**. **c** Plot of Lacunarity $L(\varepsilon)$ versus cubic gliding box size, ε. Curve fitting of the power law function to the set of Lacunarity data points obtained from the analysis of the first-, second-, and third-order Sierpinski-Menger Sponge (left to right). **d** The slope represents an estimation of the Lacunarity parameter, b, based on the linear regression of the log-transformed data for the 3 Menger sponge shown in **a**

fitted with the power law function and then taking the log transform,

$$L(\varepsilon) = a\varepsilon^b + c \tag{12}$$

$$\log_{10}\left(L(\varepsilon)' - c\right) = b log_{10}(\varepsilon) + log_{10}(a)' \tag{13}$$

where the exponent, b (referred to as the slope in a log-log plot) is related to the degree of heterogeneity in the distribution of gap sizes within the structure. A higher b value (i.e., a power law curve with wider concavity) defines higher Lacunarity, which describes a structure with a high distribution of empty gaps throughout.

In addition, the choice of the power law function is further supported by its Goodness of Fit with high R^2 values ranging between 0.9864–0.9989, RMSE between 0.0077–0.1778, and SSE between 0.0633–1.77×10^{-4} obtained from the fitting of the power law function to the 3 sets of Lacunarity

data points as shown in Fig. 2c. The results in Fig. 2d show that the Lacunarity increases from the 1st order Menger sponge (b = − 0.4748) to the 2nd order Menger Sponge (b = − 0.2536), and followed by the 3rd order Menger sponge (b = − 0.1204); highest Lacunarity amongst the 3. The trend seen in the Lacunarity plots in Fig. 2d clearly matches the observed increased heterogeneity of hole size distributions with increasing orders of the Menger sponge, thus verifying our program for Lacunarity analysis.

Figure 3 depicts four 3D blocks with parallel planes arranged in various orientations to achieve different degrees of structural anisotropy. The Succolarity analysis was performed in each of the 6 directions: serosa to mucosa (s2m), mucosa to serosa (m2s), anterior to posterior (a2p), posterior to anterior (p2a), aboral, and oral; as indicated in Fig. 3d. The calculated Succolarity values in each of the 6 directions for the 4 blocks with different degrees of anisotropy is given in Table 1. The trend seen in these values matches the observed differences in anisotropy in Fig. 3. As expected, the Succolarity of block Fig. 3a is the same in all 6 directions since the structure is isotropic, while, there is zero Succolarity in the t2b and l2r direction of block Fig. 3b and block Fig. 3c, respectively. The parallel planes in these structures, Fig. 3b and c, forms complete obstruction at the top and left boundary, respectively.

Fractal Dimension Analysis

The fractal analysis plots shown in Fig. 4 is given as log-log plots of the mean $N_{pos}(\varepsilon)$ versus ε for all identified ICC-LM, ICC-MP and ICC-CM networks over the proximal (n = 66) and distal (n = 60) cohort sets of confocal image stacks. The summary statistical analysis is presented in Table 2. The FD of the networks of ICC-LM is observed to be lower compared to the FD of the networks of ICC-MP and ICC-CM in the proximal antrum, as well as in the distal antrum (both reporting $p < 0.0001$). This is unsurprising since the ICC-LM consists of a very thin network with very sparse, striated strands (Fig. 1d). There are also markedly fewer ICC-LM that could be identified from the 126 imaged confocal stacks (n = 70) compared to ICC-MP (n = 121), and ICC-CM (n = 121). In addition, the FD values of ICC-CM were found to be significantly lower from the FDs of ICC-MP in the proximal, and in the distal antrum (both $p < 0.0001$), due to the significantly greater complexity presented by the networks of ICC-MP. In addition, the mean FD of ICC-LM networks was found to be lower in the proximal antrum compared to the distal antrum (1.30 ± 0.16 vs. 1.51 ± 0.22; $p < 0.0001$). On the other hand, the mean FD for ICC-CM networks in the proximal region was greater compared to the distal region (2.05 ± 0.08 vs. 1.89 ± 0.14; $p < 0.0001$). However, there were no observable differences found in the mean FD of ICC-MP networks between the proximal and distal antral regions (2.17 ± 0.12 vs. 2.17 ± 0.17; $p = 0.86$).

Lacunarity Analysis

As shown in Fig. 5, the corresponding Lacunarity parameter, b of the best-fit plots shown in Fig. 5 are 98.30×10^{-2} (ICC-LM), 24.52×10^{-2} (ICC-MP), and -61.54×10^{-2}

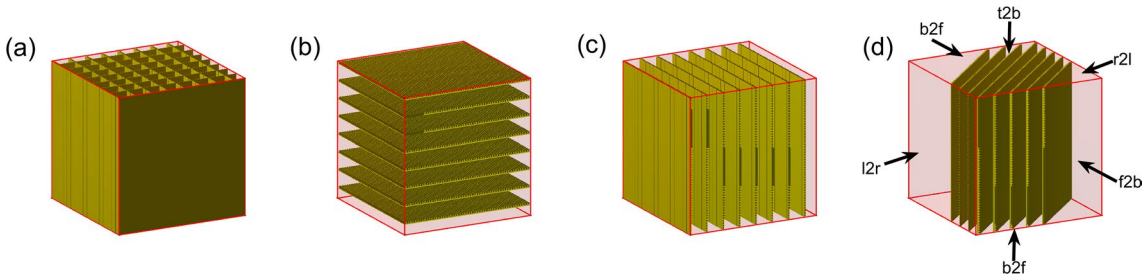

Fig. 3 Succolarity Analysis validation. The 3D structures are: **a** isotropic, **b** anisotropic in the horizontal direction, **c** anisotropic in the vertical direction, and **d** anisotropic in the diagonal direction (45°), respectively. The Succolarity analysis was perform in each of the 6 directions- top to bottom (t2b), bottom to top (b2t), left to right (l2r), right to left (r2l), front to back (f2b), and back to front (b2f); as indicated in **d**

Table 1 Succolarity validation table for a dividing factor, d = 2

Structure	t2b	b2t	l2r	r2l	f2b	b2f
(a)	0.2743	0.2743	0.2743	0.2743	0.2743	0.2743
(b)	0.0000	0.0278	0.0185	0.0185	0.0185	0.0185
(c)	0.0185	0.0185	0.0000	0.0093	0.0185	0.0185
(d)	0.0003	0.0003	0.0005	0.0002	0.0002	0.0005

Structures (a), (b), (c) and (d) are shown in Fig. 3

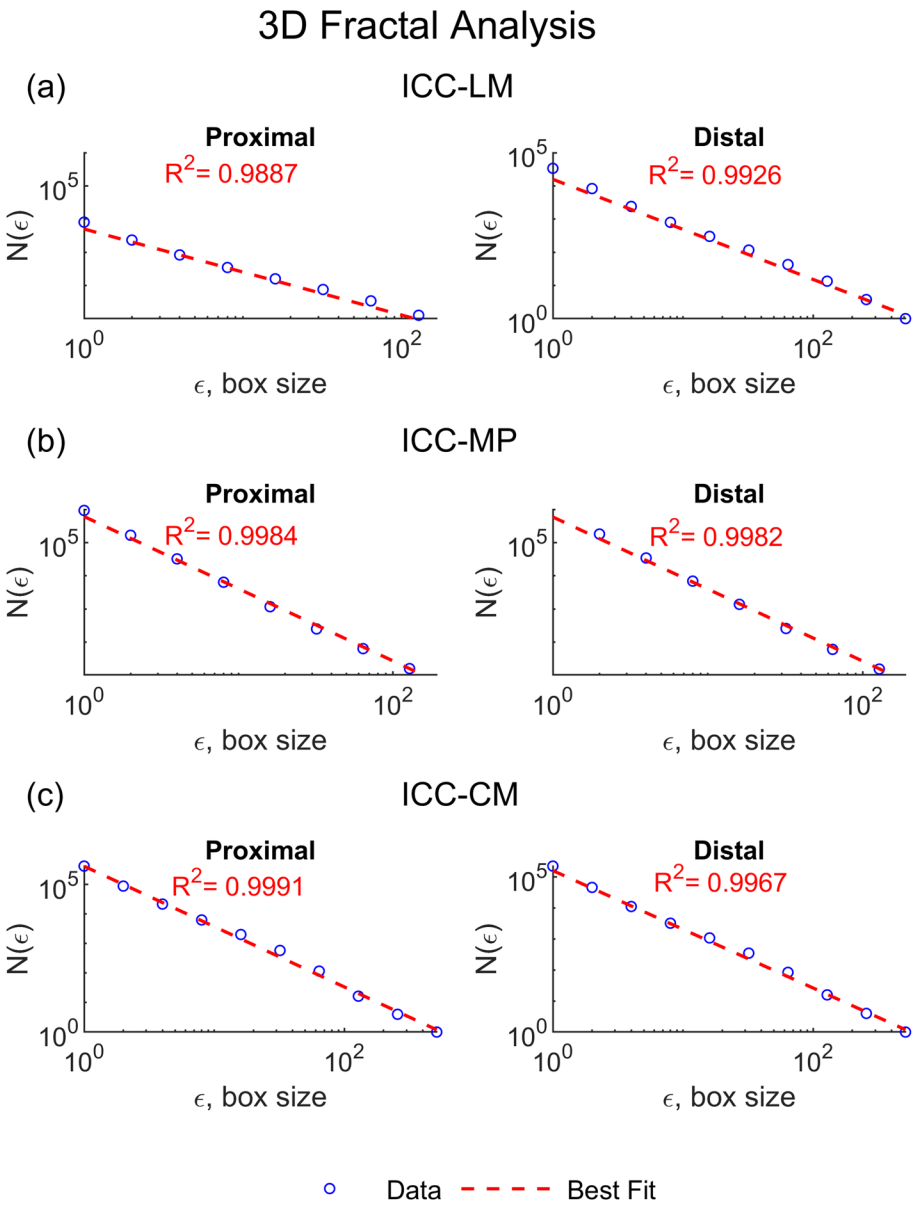

Fig. 4 Fractal Analysis. Log-log plots of the mean number of positive boxes, N(ε)of all identified **a** ICC-LM, **b** ICC-MP, and **c** ICC-CM network images across the distal and proximal murine antrum at various cubic box size, ε. The red dotted line represents the linear best fitted plot represent the overall results of the ICC-LM, ICC-MP and ICC-CM in the proximal and distal regions respectively. The slope of the best-fit line represents the mean FD of these networks

(ICC-CM) in the proximal region. On the other hand, in the distal region, the Lacunarity parameter, b are -66.65×10^{-2} (ICC-LM), -14.18×10^{-2} (ICC-MP), and -48.78×10^{-2} (ICC-CM). The wider concavity of the proximal power law curve trends infer that the Lacunarity for the networks of ICC-LM and ICC-MP, respectively is overall higher in the proximal antrum compared to the distal antrum.

The Lacunarity parameters, b for ICC-LM ($(-0.48 \pm 0.34) \times 10^{-2}$ and $(-0.54 \pm 0.52) \times 10^{-2}$) and ICC-CM ($(-0.43 \pm 0.10) \times 10^{-2}$ and $(-0.33 \pm 0.18) \times 10^{-2}$) were found to be both significantly higher than ICC-MP ($(-8.45 \pm 3.78) \times 10^{-2}$ and $(-6.47 \pm 4.53) \times 10^{-2}$) in the proximal (both reporting $p < 0.0001$) and in the distal (both reporting $p < 0.0001$) antrum, respectively.

Succolarity Analysis

Figure 6a–c depicts the variations in Succolarity of ICC-LM, ICC-MP, and ICC-CM networks, respectively along the circumferential axis of the murine gastric antrum with the vertical dotted line indicating the approximated location of the greater curvature. Details on how the approximated location of the greater curvature was registered with respect to the whole-mount proximal and distal tissue strip have been reported in Mah et al. [28].

With reference to Table 2, the Succolarity measures of ICC-LM network in the aboral direction throughout the circumferential axis were found to be consistently higher in the proximal than in the distal antrum ($2.49 \pm 3.94 \times 10^{-4}$ vs. $0.71 \pm 3.03 \times 10^{-4}$; $p = 0.0416$). As shown in Fig. 6b,

Table 2 Statistical summary table for two-sample t test

Groups	ICC-LM		ICC-MP		ICC-CM	
Regions	Proximal	Distal	Proximal	Distal	Proximal	Distal
Fractal dimension (FD)	1.30 ± 0.16 $p = 1.3724 \times 10^{-5}$	1.51 ± 0.22	2.17 ± 0.12 $p = 0.8610$	2.17 ± 0.17	2.05 ± 0.08 $p = 6.2741 \times 10^{-11}$	1.89 ± 0.14
Lacunarity parameter (b) ($\times 10^{-2}$)	-0.48 ± 0.34 $p = 0.6907$	-0.54 ± 0.52	-8.45 ± 3.78 $p = 0.0115$	-6.47 ± 4.53	-0.43 ± 0.10 $p = 4.2391 \times 10^{-4}$	-0.33 ± 0.18
Succolarity (σ) ($\times 10^{-4}$)						
s2m	0.90 ± 0.15 $p = 0.0120$	0.26 ± 1.47	332 ± 754 $p = 0.7602$	291 ± 717	1.63 ± 6.51 $p = 0.1537$	0.47 ± 0.18
m2s	1.96 ± 3.76 $p = 0.5378$	1.43 ± 3.33	1465 ± 1285 $p = 3.4818 \times 10^{-5}$	656 ± 741	5.50 ± 11 $p = 0.0860$	2.90 ± 5.60
a2p	0.96 ± 2.37 $p = 0.5407$	1.35 ± 2.94	1258 ± 1069 $p = 1.9663 \times 10^{-6}$	500 ± 534	5.24 ± 9.68 $p = 0.0527$	2.63 ± 4.44
p2a	0.35 ± 1.06 $p = 0.5181$	0.21 ± 0.46	1053 ± 1080 $p = 2.9043 \times 10^{-4}$	474 ± 581	3.25 ± 8.28 $p = 0.0286$	0.91 ± 1.76
Oral	0.83 ± 0.25 $p = 0.8742$	0.92 ± 3.35	1044 ± 1144 $p = 4.2930 \times 10^{-4}$	455 ± 589	0.46 ± 2.36 $p = 0.6773$	0.32 ± 1.16
Aboral	2.49 ± 3.94 $p = 0.0416$	0.71 ± 3.03	1265 ± 1155 $p = 2.2332 \times 10^{-5}$	544 ± 577	8.17 ± 18 $p = 0.0046$	1.49 ± 3.69
Mean	1.25 ± 1.17 $p = 0.1396$	0.81 ± 1.26	1069 ± 788 $p = 2.1450 \times 10^{-6}$	486 ± 477	4.04 ± 5.53 $p = 5.8223 \times 10^{-4}$	1.45 ± 1.82

Succolarity values of ICC-MP network in all 6 directions are predominantly higher in the proximal antrum compared to the distal antrum throughout the circumferential axis. In particular, the proximal versus distal Succolarity values of the ICC-MP network are within $(1465 \pm 1285) \times 10^{-4}$ vs. $(656 \pm 741) \times 10^{-4}$; (in the direction from m2s), $(1258 \pm 1069) \times 10^{-4}$ vs. $(500 \pm 534) \times 10^{-4}$; (in the direction from a2p), $(1053 \pm 1080) \times 10^{-4}$ vs. $(474 \pm 581) \times 10^{-4}$; (in the direction from p2a), $(1044 \pm 1144) \times 10^{-4}$ vs. $(455 \pm 589) \times 10^{-4}$; (in the aboral direction), and $(1265 \pm 1155) \times 10^{-4}$ vs. $(544 \pm 577) \times 10^{-4}$; (in the oral direction).

In the proximal antrum, Succolarity of ICC-MP in all directions, in general appears to be the highest near the greater curvature with average Succolarity measures of 0.0930 (s2m), 0.2905 (m2s), 0.2348 (a2p), 0.1510 (p2a), 0.1737 (aboral), and 0.2422 (oral). On the other hand, in the distal antrum the ICC-MP Succolarity measures in all six directions demonstrated a gradual increase along the circumferential axis from the anterior side towards the posterior side of the gastric antrum (Fig. 6b). The increase in Succolarity of ICC-MP network in the distal antrum is by 705×10^{-4}, 986×10^{-4}, 789×10^{-4}, 222×10^{-4}, 563×10^{-4}, and 799×10^{-4} in the s2m, m2s, a2p, p2a, aboral, and oral direction, respectively; and over a span of 2513.8 µm proceeding from the greater curvature towards the lesser curvature of the posterior antrum (Fig. 6b).

Conversely, the Succolarity of ICC-CM in the proximal antrum, as observed in Fig. 6c, appears to gradually decrease along the circumferential axis from the anterior side towards the posterior side of the gastric antrum. The decline in Succolarity of ICC-CM network in the proximal is by 17.2×10^{-4}, 23.3×10^{-4}, 24.6×10^{-4}, 17.6×10^{-4}, 0.296×10^{-4}, 28.6×10^{-4} in the s2m, m2s, a2p, p2a, aboral, and oral direction, respectively, over a span of 1955.1 µm proceeding from the lesser curvature towards the greater curvature of the anterior antrum (Fig. 6c). A similar trend is observed as to the Succolarity of ICC-MP network; likewise, the Succolarity of ICC-CM network is overall higher in the proximal antrum compared to the distal antrum. However, the differences are less pronounced compared to that of ICC-MP Succolarity measures. In the proximal antrum, the Succolarity of ICC-CM networks were computed to be within $(1.63 \pm 6.51) \times 10^{-4}$ (s2m), $(5.50 \pm 11) \times 10^{-4}$ (m2s), $(5.24 \pm 9.68) \times 10^{-4}$ (a2p), $(3.25 \pm 8.28) \times 10^{-4}$ (p2a), $(0.46 \pm 2.36) \times 10^{-4}$ (aboral), and $(8.17 \pm 18) \times 10^{-4}$ (oral). On the other hand, in the distal antrum, the Succolarity of ICC-CM networks were computed to be within $(0.47 \pm 0.18) \times 10^{-4}$ (s2m), $(2.90 \pm 5.60) \times 10^{-4}$ (m2s), $(2.63 \pm 4.44) \times 10^{-4}$ (a2p), $(0.91 \pm 1.76) \times 10^{-4}$ (p2a), $(0.32 \pm 1.16) \times 10^{-4}$ (aboral), and $(1.49 \pm 3.69) \times 10^{-4}$ (oral).

With reference to the box-plots in Fig. 7, the Succolarity of the networks of ICC-LM in the proximal antrum was significantly lower in the p2a direction $((0.35 \pm 1.06) \times 10^{-4})$ than in the oral direction $((2.49 \pm 3.94) \times 10^{-4})$ with $p = 0.0096$. The Succolarity of the networks of ICC-MP in the proximal antrum was significantly lower in the

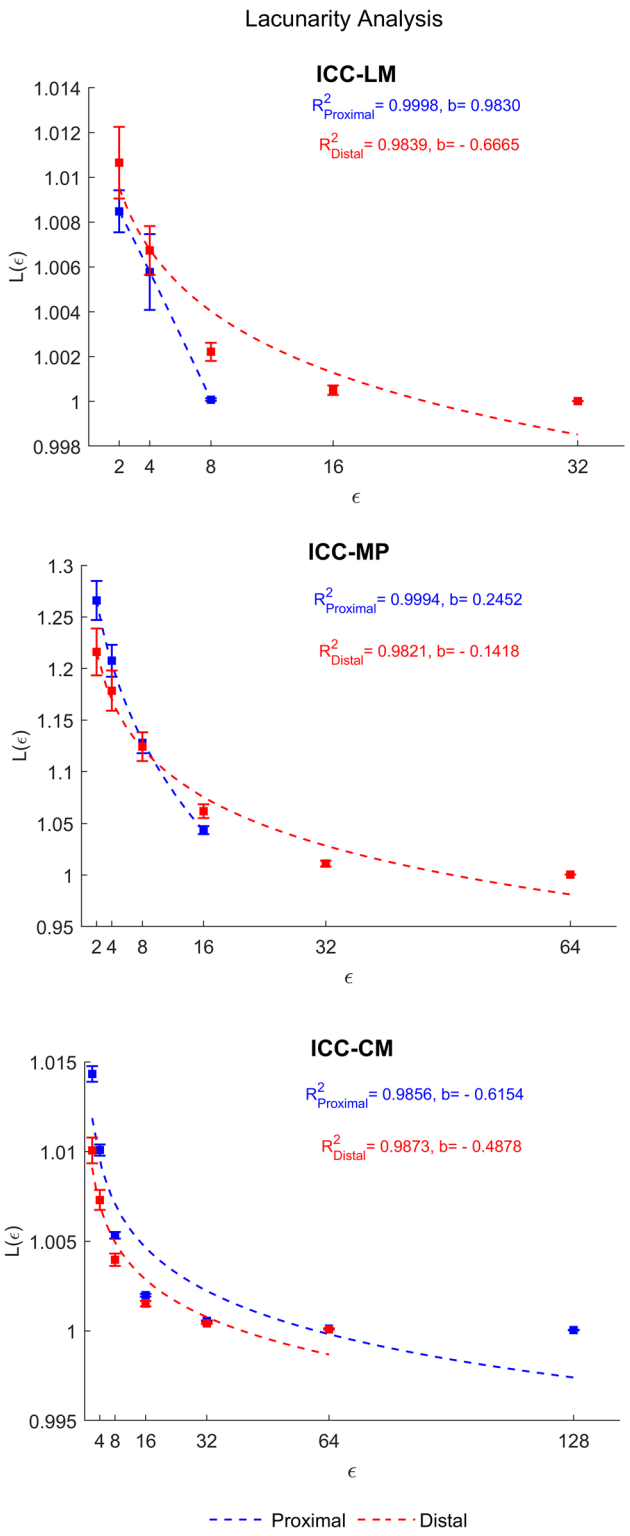

Fig. 5 Lacunarity Analysis. Log-log plots for the mean Lacunarity of all identified ICC-LM, ICC-MP & ICC-CM networks from the 66 proximal and 60 distal antral confocal image stacks. The slope of the best fit linear plots represents the overall mean Lacunarity parameter which is used the gauge the extent in the distribution of empty gaps throughout the network structure

s2m direction $(332 \pm 754) \times 10^{-4}$ compared to the other 5 directions investigated- m2s $((1465 \pm 1285) \times 10^{-4}$; $p < 0.0001$), a2p $((1258 \pm 1069) \times 10^{-4}$; $p < 0.0001$), p2a $((1053 \pm 1080) \times 10^{-4}$; $p = 0.0026$), aboral $((1044 \pm 1144) \times 10^{-4}$; $p = 0.0031$), and oral direction $((1265 \pm 1155) \times 10^{-4}$; $p < 0.0001$). On the other hand, the Succolarity of the networks of ICC-MP in the distal antrum was found to be significantly lower in the s2m direction $(291 \pm 717) \times 10^{-4}$ compared to the m2s direction only $((656 \pm 741) \times 10^{-4}$; $p = 0.0373$). The Succolarity of the networks of ICC-CM in the proximal antrum was found to be significantly higher in the oral direction $((8.17 \pm 18) \times 10^{-4})$ compared to the s2m direction $((1.63 \pm 6.51) \times 10^{-4}$; $p = 0.0051$) and aboral direction $((0.46 \pm 2.36) \times 10^{-4}$; $p < 0.001$). While, in the distal antrum, the Succolarity of the network of ICC-CM was found to be significantly higher in the m2s direction $((2.90 \pm 5.60) \times 10^{-4})$ than in the s2m direction $((0.47 \pm 0.18) \times 10^{-4}$; $p = 0.0031$), p2a direction $((0.91 \pm 1.76) \times 10^{-4}$; $p = 0.0343$), and aboral direction $((0.32 \pm 1.16) \times 10^{-4}$; $p = 0.0012$). Furthermore, the Succolarity of the network of ICC-CM in the distal antrum was found to be significantly higher in the a2p direction $((2.63 \pm 4.44) \times 10^{-4})$ than in the s2m direction ($p = 0.0146$), and in the aboral direction ($p = 0.0063$).

The results of the two-sample t-test are summarized in Table 2. The Fractal Dimensions of ICC-LM and ICC-CM between the proximal and distal antrum regions were significantly different with both reporting $p < 0.0001$. While no significant difference was found between the proximal and distal antrum regions for the FD of ICC-MP ($p = 0.8610$). The Lacunarity parameter, b of ICC-MP and ICC-CM between the proximal and distal antrum regions were significantly different with $p = 0.0115$ and $p < 0.001$, respectively. However, no significant difference was found between the proximal and distal antrum regions for the Lacunarity parameter, b of ICC-LM ($p = 0.6907$). The Succolarity of ICC-LM between the proximal and distal antrum regions in the direction from serosa to mucosa (s2m), and distal to proximal (oral) were significantly different with $p = 0.0120$ and $p = 0.0416$, respectively. On the other hand, no significant difference was found between the proximal and distal antrum regions for the Succolarity of ICC-LM in the other 4 directions analyzed- m2s ($p = 0.5378$), a2p ($p = 0.5407$), p2a ($p = 0.5181$), aboral ($p = 0.8742$). The Succolarity of ICC-MP in the proximal antrum regions of the 5 directions analyzed were significantly higher than the distal regions with $p < 0.0001$ (m2s), $p < 0.0001$ (a2p), $p < 0.001$ (p2a), $p < 0.001$ (aboral), and $p < 0.0001$ (oral). However, no significant difference was found between the proximal and distal antrum regions for the Succolarity of ICC-MP in the direction of s2m ($p = 0.7602$). The Succolarity of ICC-CM between the proximal and distal antrum regions in the direction from p2a, and distal to proximal (oral) were significantly different with $p = 0.0286$

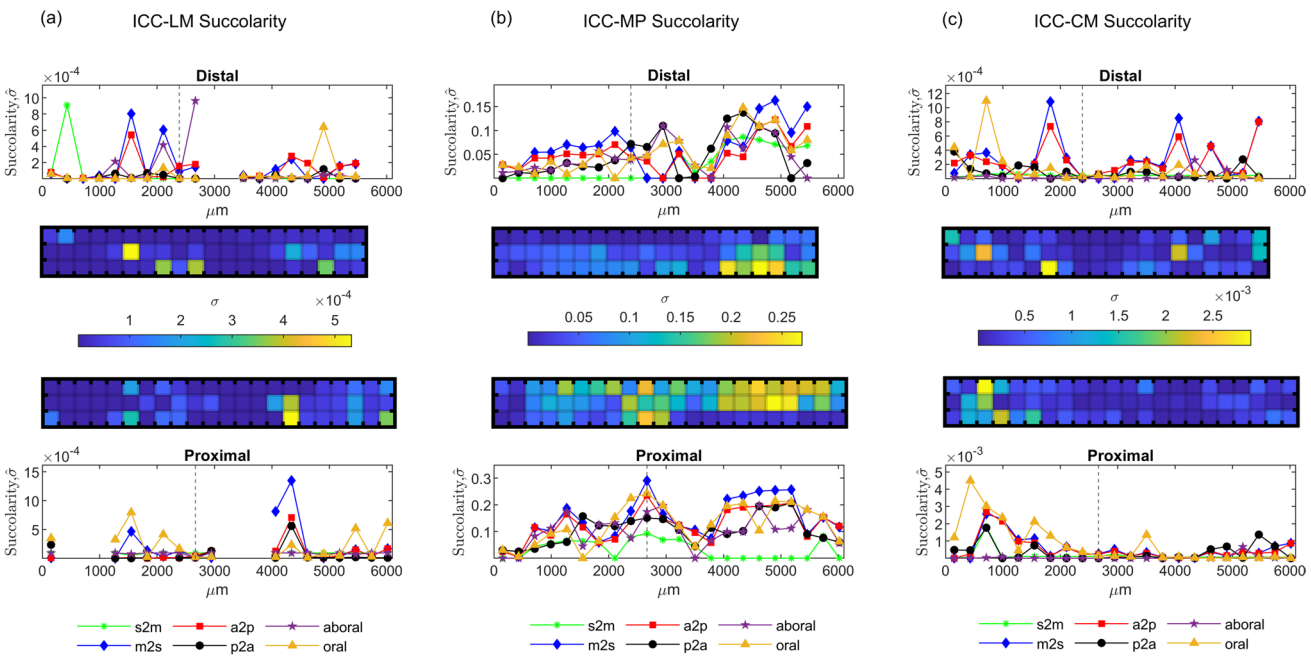

Fig. 6 Succolarity results of the 3 types of ICC network structures: **a** ICC-LM, **b** ICC-MP, **c** ICC-CM across the distal and proximal murine antrum in the 6 directions analyzed with a dividing factor, d = 2 (BS = 2 × 2 × 2). The vertical dotted line indicates the approximated location of the greater curvature- the border that separates between the anterior (left) and the posterior (right) antral surfaces. The directions of Succolarity analyzed with respect to the whole-mount confocal antral tissue are- serosal to mucosa (s2m), mucosa to serosal (m2s), anterior to posterior (a2p), posterior to anterior (p2a), proximal to distal (aboral), distal to proximal (oral)

and p = 0.0046, respectively. Conversely, no significant difference was found between the proximal and distal antrum regions for the Succolarity of ICC-CM in the other 4 directions analyzed—s2m (p = 0.1537), m2s (p = 0.0860), a2p (p = 0.0527), and aboral (p = 0.6773).

Discussion

The current study presents a systematic and in-depth evaluation of the FD, Lacunarity, and Succolarity to characterize structural ICC network complexity from confocal image datasets, and may present a potential tool for diagnosing changes in ICC associated with FGIDs [3, 15, 24, 40]. These fractal parameters have shown potential capabilities to capture the dynamics of complex physiologic networks and therefore, aid our theoretical understanding of organisms functions in health and disease [41].

Fractal analyses has been used to characterize physiological processes [7, 21, 37], as well as anatomical structures [12] (e.g., pulmonary and myocardial blood flow, bronchial, and vascular tree structures [17, 32]). Fractal analysis has the potential to provide a comprehensive and nuanced understanding of the ICC network structure, function, and dynamics affecting gut motility, which could provide new insights into GI disorders and, develop new approaches to diagnosis and treatment. The fractal properties of the network structure may reflect the propagation of SWs and the coordination of myogenic contractions along the GI tact. The geometry of the ICC network in the gastric tissue sections were empirically measured through a combination of FD, Lacunarity, and Succolarity analyses. These analyses provide us with quantitative and qualitative measures, and their evaluation does not require priori experience. The FD characterize the extent of geometric complexity and branching self-similarity of the ICC network, while Lacunarity provide a measure of the degree of geometric diversity or heterogeneity in distribution of the ICC network structure caused by the presence of gaps within the structure. The mean FD of ICC-MP network is significantly greater compared to the mean FD of ICC-LM and ICC-CM networks throughout the gastric antrum. In addition, the overall web like ICC-MP networks have predominantly higher Lacunarity compared to that of the striated ICC-LM and ICC-CM networks.

The unique feature of Succolarity is useful for distinguishing anatomical structures with some directional or flow information associated with it that cannot be discriminated by neither FD nor Lacunarity [6]. Succolarity can be used as a measure of geometric connectivity of the ICC network in a particular direction, and therefore indicates the propensity of SWs to actively propagate in that direction via the ICC structure to generate a particular motility pattern

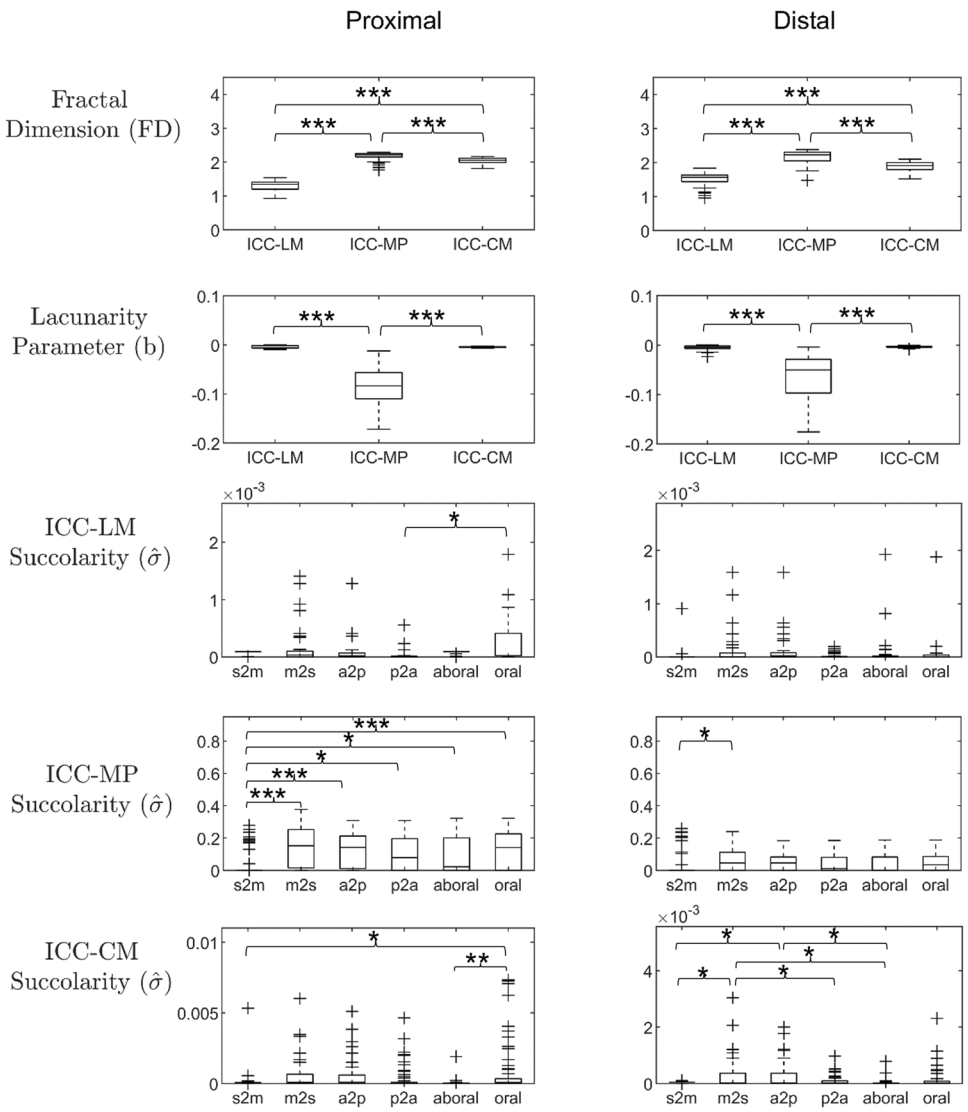

Fig. 7 One-way ANOVA: Statistical analysis performed for ICC-LM, ICC-MP, and ICC-CM in the proximal and distal antral regions, respectively for each fractal parameter. The Succolarity was evaluated in the direction from: - serosa to mucosa (s2m), mucosa to serosa (m2s), anterior to posterior (a2p), posterior to anterior (p2a), and in the aboral, oral directions; respectively. A statistically significant difference was found in 9 sub-figures (***$p < 0.0001$, **$p < 0.001$, *$p < 0.05$). A plus symbol in the boxplot represents an outlier

from resultant myoelectrical contractions. This present study emphasizes the significance of ICC structural connectivity on slow wave propagation, supported by compelling evidence from previous research [8, 10]. The Succolarity measures of ICC-LM network in the aboral direction were found to be consistently higher in the proximal than in the distal antrum; suggesting that the intensity of longitudinal muscle contractions decreases aborally towards the terminal antrum possibly to restrict digesta from accelerating pass the pyloric region [26]. Extracellular mapping studies have demonstrated increased SW amplitude (stronger activity) and velocity in the prepyloric antrum [4]. Thus, we hypothesized that increasingly rapid large circumferential muscle contractions is responsible for increasing antral recirculation to enhance gastric mixing at the terminal antrum. Further investigations coupling the structural element with slow wave propagation simulations are required to fully comprehend this relationship.

The FD and Lacunarity parameter, b estimates obtained from the box-counting and gliding box algorithm will numerically depend on the ε-range over which the linear regression of the log-transformed data is computed. In this study, FD and Lacunarity parameter, b were estimated over the scale interval of $\varepsilon = 2$ to 512 and $\varepsilon = 2$ to 32, respectively, however; the question remains as to which ε-range will adequately or best capture the underlying FD and b estimates. The validation studies of Sierpinski-Menger sponge sets ("Algorithm Verification" section) demonstrate adequate estimation accuracy for FD (RMSE = 0.1484) with an ε-range between 2 to 512 (Fig. 2b), and Lacunarity parameter, b estimates (RMSE between 0.0077–0.1778) over an ε-range between 2 to 32 (Fig. 2c, d). However, a particular scale interval that yields good estimation accuracy for one type of structure may not necessarily fare equally well for another type of structure [23]. Furthermore, the set of Menger sponges only differed from each other over an order,

while the ICC network segmentations may differ over many degrees of freedom for different ICC types, regions, and sequences. To obtain an optimized estimation, Krohn et al. [23] applied an algorithmic scale optimization procedure that can improve the estimation accuracy, as well as, demonstrates increased flexibility toward different object types.

While our study demonstrates that by combining Succolarity, Lacunarity, and Fractal Dimension analysis, it is possible to quantitatively characterize ICC network structures to provide a better understanding on the influence of complexity, self-similarity, heterogeneity, and anisotropy of structural properties to physiological function, a wider range of confocal imaging data, as well as, from more subjects would offer a more comprehensive analysis of the spatial variations of the ICC networks. We seek to resolve these limitations and plan to analyze the confocal images along with corresponding SW signals recorded from the same mouse imaged in future studies. The Hurst exponent—another fractal parameter, is a measure of the long-term correlation or self-similarity of a signal [7]. Analysis of the SW signals with the Hurst exponent, from control mice and mice with different levels of GI dysmotility can provide complementary information about the degree of persistence or anti-persistence in the SW signal, thereby reflecting the underlying physiological and pathological processes affecting gut motility. A high Hurst exponent may indicate a more organized and coordinated SW activity that is associated with normal GI motility, while, a significantly lower Hurst exponent may imply a more disorganized and erratic SW activity, that indicate impaired motility.

Any pathological morphology should exhibit decreased complexity- marks a physiologic network's response, measured by FD [13], and can be used as an indicator of the state of health. This hypothesis has been well supported by numerous studies [18, 34, 38]. For example, Stosic and Stosic [38] observed that retinal vascular networks associated with various pathological processes expressed a significantly lower generalized FD- lower complexity, compared to retinal vascular networks of healthy people. In addition, a number of investigators have reported sparse, less complex (lower FD) retina microvasculature in hypertensive retinopathy, diabetic retinopathy, and in Alzheimer's disease [18, 23, 34]. As such, a higher FD may indicate a more complex and interconnected ICC network that is associated with normal motility, while a lower FD may indicate a less complex and fragmented ICC network that is associated with impaired motility. We seek to test out this hypothesis in our impending future studies between healthy subjects and those with GI dysmotility. At present, this exploratory study demonstrates that the network of ICC-MP is highly complex relative to the striated strands of ICC-LM and ICC-CM networks through the significantly greater FD measured throughout. In addition, the mean FD of ICC-LM networks was found to be lower in the proximal compared to the distal antrum but appears vice-versa for the mean FD of ICC-CM networks. Hence, FD may also be used to distinguish between these two smooth muscle networks.

The study presented here provides valuable insights into the complex network structure of ICC in GI tissues. There is potential for assimilating these findings into mathematical models of GI slow waves, by incorporating the fractal analysis parameters into structural simulations of ICC networks. The integration of empirical data and mathematical modeling holds promise for unravelling the complexities of ICC networks and shedding light on the functional significance of their structural characteristics [25]. However, it is important to note that further experimental studies and investigations are required to validate the clinical translation and applicability of these fractal indices (i.e. FD, Lacunarity, Succolarity) in the context of GI dysmotility and disease diagnostics. This multidisciplinary approach, combining experimental techniques, electrophysiological recordings, and computational modeling, can lead to comprehensive insights into disease mechanisms and potential treatment strategies, fostering advancements in FGIDs diagnosis and management.

Conclusion

Our findings raise hopes of defining novel biomarkers for improved diagnostics and enhancing our understanding of disease-induced ICC network changes/remodeling. To achieve this goal, however, the diagnostics and prognostic capacity of fractal analysis needs further investigation, both on a diseased population with varying degrees of GI dysmotility and on healthy controls. As such, future work is warranted to expand upon the utility of our present fractal analysis for gastric histopathological imaging; specifically with respect to disease diagnostics. Thus, this present work contributes to the methodological groundwork to facilitate progress in this direction.

Acknowledgements The authors thank Perrine Hagué, Faculté de Médecine, Université Libre de Bruxelles, Belgium for technical assistance in mice breeding and tissue clearing, and Prof. Dieter Saur, School of Medicine, Technische Universität München, Germany for providing the KitCreERT2, R26mT-mG mice colony founders.

Author Contributions Author SM conducted the conception of the study, technical analysis & statistic, and wrote the manuscript. JM provided the microscopic imaging data. RA and PD supervised the project. All authors took part in reviewing and editing the manuscript.

Funding This work was supported, in part, by grants from the Marsden Fund Council and Rutherford Foundation managed by The Royal Society Te Apārangi.

Data availability Not applicable.

Declarations

Conflict of interest The authors declare that the research was conducted in the absence of any commercial or financial relationships that could be construed as a potential conflict of interest.

References

1. Abdelsalam, M. M., and M. A. Zahran. A novel approach of diabetic retinopathy early detection based on multifractal geometry analysis for OCTA macular images using support vector machine. *IEEE Access*. 9:22844–22858, 2021.
2. An, W., C. Wang, H. Zhang, and Z. Bi. Measuring the formal complexity of architectural curved surfaces based on 3D box-counting dimension. *Nexus Netw. J.* 24:753–766, 2022.
3. Angeli, T. R., L. K. Cheng, P. Du, T.H.-H. Wang, C. E. Bernard, M.-G. Vannucchi, M. S. Faussone-Pellegrini, C. Lahr, R. Vather, J. A. Windsor, G. Farrugia, T. L. Abell, and G. O'Grady. Loss of interstitial cells of cajal and patterns of gastric dysrhythmia in patients with chronic unexplained nausea and vomiting. *Gastroenterology*. 149:56-66.e5, 2015.
4. Berry, R., T. Miyagawa, N. Paskaranandavadivel, P. Du, T. R. Angeli, M. L. Trew, J. A. Windsor, Y. Imai, G. O'Grady, and L. K. Cheng. Functional physiology of the human terminal antrum defined by highresolution electrical mapping and computational modeling. *Am. J. Physiol.-Gastrointest Liver Physiol.* 311:G895–G902, 2016.
5. Bunde, A., and S. Havlin. Fractals in Science. Berlin: Springer, 2013. https://doi.org/10.1007/978-3-642-77953-4.
6. De Melo, R. H. C., and A. Conci. How succolarity could be used as another fractal measure in image analysis. *Telecommun. Syst.* 52:1643–1655, 2013.
7. DePetrillo, P. B., D. Speers, and U. E. Ruttimann. Determining the Hurst exponent of fractal time series and its application to electrocardiographic analysis. *Comput. Biol. Med.* 29:393–406, 1999.
8. Du, P., G. O'Grady, S. J. Gibbons, R. Yassi, R. Lees-Green, G. Farrugia, L. K. Cheng, and A. J. Pullan. Tissue-specific mathematical models of slow wave entrainment in wild-type and 5-HT(2B) knockout mice with altered interstitial cells of Cajal networks. *Biophys. J.* 98:1772–1781, 2010.
9. Gao, J., P. Du, G. O'Grady, R. Archer, G. Farrugia, S. J. Gibbons, and L. K. Cheng. Numerical metrics for automated quantification of interstitial cell of Cajal network structural properties. *J. R. Soc. Interface*. 10:20130421, 2013.
10. Gao, J., P. Du, G. O'Grady, R. Archer, S. J. Gibbons, G. Farrugia, and L. K. Cheng. Cellular automaton model for simulating tissue-specific intestinal electrophysiological activity. *Conf. Proc. ... Annu. Int. Conf. IEEE Eng. Med. Biol. Soc. IEEE Eng. Med. Biol. Soc. Annu. Conf.* 5537–5540, 2013.
11. Gkontra, P., K. A. Norton, M. M. Zak, C. Clemente, J. Agüero, B. Ibáñez, A. Santos, A. S. Popel, and A. G. Arroyo. Deciphering microvascular changes after myocardial infarction through 3D fully automated image analysis. *Sci. Rep.* 81(8):1–19, 2018.
12. Glenny, R. W., H. T. Robertson, S. Yamashiro, and J. B. Bassingthwaighte. Applications of fractal analysis to physiology. *J. Appl. Physiol.* 70:2351–2367, 1991.
13. Goldberger, A. L. Fractal variability versus pathologic periodicity: Complexity loss and stereotypy in disease. *Perspect. Biol. Med.* 40:543–561, 1997.
14. Gould, D. J., T. J. Vadakkan, R. A. Poché, and M. E. Dickinson. Multifractal and lacunarity analysis of microvascular morphology and remodeling. *Microcirculation*. 18:136–151, 2011.
15. Grover, M., G. Farrugia, M. S. Lurken, C. E. Bernard, M. S. Faussone-Pellegrini, T. C. Smyrk, H. P. Parkman, T. L. Abell, W. J. Snape, W. L. Hasler, A. Ünalp-Arida, L. Nguyen, K. L. Koch, J. Calles, L. Lee, J. Tonascia, F. A. Hamilton, and P. J. Pasricha. Cellular changes in diabetic and idiopathic gastroparesis. *Gastroenterology*. 140:1575–1585, 2011.
16. He, C. L., L. Burgart, L. Wang, J. Pemberton, T. Young-Fadok, J. Szurszewski, and G. Farrugia. Decreased interstitial cell of cajal volume in patients with slow-transit constipation. *Gastroenterology*. 118:14–21, 2000.
17. Horsfield, K. Morphometry of the small pulmonary arteries in man. *Circ. Res.* 42:593–597, 1978.
18. Hughes, A. D., E. Martinez-Perez, A.-S. Jabbar, A. Hassan, N. W. Witt, P. D. Mistry, N. Chapman, A. V. Stanton, G. Beevers, R. Pedrinelli, K. H. Parker, and S. A. M. M. Thom. Quantification of topological changes in retinal vascular architecture in essential and malignant hypertension. *J. Hypertens.* 24:889–894, 2006.
19. Huizinga, J. D., N. Zarate, and G. Farrugia. Physiology, injury, and recovery of interstitial cells of Cajal: basic and clinical science. *Gastroenterology*. 137:1548–1556, 2009.
20. Isozaki, K., S. Hirota, J. Miyagawa, M. Taniguchi, Y. Shinomura, and Y. Matsuzawa. Deficiency of c-kit+ cells in patients with a myopathic form of chronic idiopathic intestinal pseudo-obstruction. *Am. J. Gastroenterol.* 92:332–334, 1997.
21. Julián, M., R. Alcaraz, and J. J. Rieta. Application of Hurst exponents to assess atrial reverse remodeling in paroxysmal atrial fibrillation. *Physiol. Meas.* 36:2231, 2015.
22. Klein, S., B. Seidler, A. Kettenberger, A. Sibaev, M. Rohn, R. Feil, H.-D. Allescher, J.-M. Vanderwinden, F. Hofmann, M. Schemann, R. Rad, M. A. Storr, R. M. Schmid, G. Schneider, and D. Saur. Interstitial cells of Cajal integrate excitatory and inhibitory neurotransmission with intestinal slow-wave activity. *Nat. Commun.* 4:1630, 2013.
23. Krohn, S., M. Froeling, A. Leemans, D. Ostwald, P. Villoslada, C. Finke, and F. J. Esteban. Evaluation of the 3D fractal dimension as a marker of structural brain complexity in multiple-acquisition MRI. *Hum. Brain Mapp.* 40:3299–3320, 2019.
24. Lee, J., II., H. Park, M. A. Kamm, and I. C. Talbot. Decreased density of interstitial cells of Cajal and neuronal cells in patients with slow-transit constipation and acquired megacolon. *J. Gastroenterol. Hepatol.* 20:1292–8, 2005.
25. Mah, S. A., R. Avci, L. K. Cheng, and P. Du. Current applications of mathematical models of the interstitial cells of Cajal in the gastrointestinal tract. *WIREs Mech. Dis.*13:e1507, 2021.
26. Mah, S. A., R. Avci, P. Du, J.-M. Vanderwinden, and L. K. Cheng. Antral variation of murine gastric pacemaker cells informed by confocal imaging and machine learning methods. *Annu. Int. Conf. IEEE Eng. Med. Biol. Soc. IEEE Eng. Med. Biol. Soc. Annu. Int. Conf.* 2021:3105–3108, 2021.
27. Mah, S. A., R. Avci, P. Du, J. M. Vanderwinden, and L. K. Cheng. Deciphering stomach myoelectrical slow wave conduction patterns via confocal imaging of gastric pacemaker cells and fractal geometry. *Annu. Int. Conf. IEEE Eng. Med. Biol. Soc. IEEE Eng. Med. Biol. Soc. Annu. Int. Conf.* 2022:3514–3517, 2022.
28. Mah, S. A., P. Du, R. Avci, J.-M. Vanderwinden, and L. K. Cheng. Analysis of regional variations of the interstitial cells of Cajal in the Murine distal stomach informed by confocal imaging and machine learning methods. *Cell. Mol. Bioeng.* 15:193–205, 2022.
29. Mandelbrot, B. B. The Fractal Geometry of Nature. San Francisco: W.H. Freeman and Company, pp. 394–397, 1982.
30. Masters, B. R. Fractal analysis of the vascular tree in the human retina. *Annu. Rev. Biomed. Eng.* 6:427–452, 2004.
31. Murueta-Goyena, A., M. Barrenechea, A. Erramuzpe, S. Teijeira-Portas, M. Pengo, U. Ayala, D. Romero-Bascones, M. Acera, R. Del Pino, J. C. Gómez-Esteban, and I. Gabilondo. Foveal

remodeling of retinal microvasculature in Parkinson's disease. *Front. Neurosci.* 15:837, 2021.
32. Nelson, T. R., and D. K. Manchester. Modeling of lung morphogenesis using fractal geometries. *IEEE Trans. Med. Imaging*. 7:321–327, 1988.
33. O'Grady, G., P. Du, L. K. Cheng, J. U. Egbuji, W. J. E. P. Lammers, J. A. Windsor, and A. J. Pullan. Origin and propagation of human gastric slow-wave activity defined by high-resolution mapping. *Am. J. Physiol. Gastrointest. Liver Physiol.* 299:G585–G592, 2010.
34. Popovic, N., M. Radunovic, J. Badnjar, and T. Popovic. Fractal dimension and lacunarity analysis of retinal microvascular morphology in hypertension and diabetes. *Microvasc. Res.* 118:36–43, 2018.
35. Rolle, U., A. P. Piotrowska, L. Nemeth, and P. Puri. Altered distribution of interstitial cells of Cajal in Hirschsprung disease. *Arch. Pathol. Lab. Med.* 126:928–933, 2002.
36. Smith, T. G., W. B. Marks, G. D. Lange, W. H. Sheriff, and E. A. Neale. A fractal analysis of cell images. *J. Neurosci. Methods*. 27:173–180, 1989.
37. Souza França, L. G., J. G. Vivas Miranda, M. Leite, N. K. Sharma, M. C. Walker, L. Lemieux, and Y. Wang. Fractal and multifractal properties of electrographic recordings of human brain activity: toward its use as a signal feature for machine learning in clinical applications. *Front. Physiol.* 9:1767, 2018.
38. Stošić, T., and B. D. Stošić. Multifractal analysis of human retinal vessels. *IEEE Trans. Med. Imaging*. 25:1101–1107, 2006.
39. Tolle, C. R., T. R. McJunkin, and D. J. Gorsich. An efficient implementation of the gliding box lacunarity algorithm. *Phys. D Nonlinear Phenom.* 237:306–315, 2008.
40. Vanderwinden, J.-M., and J. J. Rumessen. Interstitial cells of Cajal in human gut and gastrointestinal disease. *Microsc. Res. Tech.* 47:344–360, 1999.
41. West, B. J. Fractal physiology and the fractional calculus: a perspective. *Front. Physiol.* 1:12, 2010.
42. Wu, J., X. Jin, S. Mi, and J. Tang. An effective method to compute the box-counting dimension based on the mathematical definition and intervals. *Results Eng.*6:100106, 2020.
43. Xia, Y., J. Cai, E. Perfect, W. Wei, Q. Zhang, and Q. Meng. Fractal dimension, lacunarity and succolarity analyses on CT images of reservoir rocks for permeability prediction. *J. Hydrol.*579:124198, 2019.